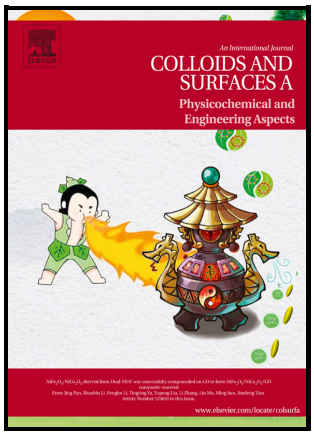

Protein encapsulation in mesoporous silica: influence of the mesostructured and pore wall properties

Rémi G. Tilkin, Julien G. Mahy, Ana P.F. Monteiro, Artium Belet, Julio Feijóo, Mathilde Laird, Carole Carcel, Nicolas Régibeau, Bart Goderis, Christian Grandfils, Michel Wong Chi Man, Stéphanie D. Lambert

PII: S0927-7757(22)00383-1

DOI: https://doi.org/10.1016/j.colsurfa.2022.128629

Reference: COLSUA128629

To appear in: *Colloids and Surfaces A: Physicochemical and Engineering Aspects*

Received date: 16 December 2021
Revised date: 11 February 2022
Accepted date: 20 February 2022

Please cite this article as: Rémi G. Tilkin, Julien G. Mahy, Ana P.F. Monteiro, Artium Belet, Julio Feijóo, Mathilde Laird, Carole Carcel, Nicolas Régibeau, Bart Goderis, Christian Grandfils, Michel Wong Chi Man and Stéphanie D. Lambert, Protein encapsulation in mesoporous silica: influence of the mesostructured and pore wall properties, *Colloids and Surfaces A: Physicochemical and Engineering Aspects,* (2021) doi:https://doi.org/10.1016/j.colsurfa.2022.128629

Protein encapsulation in mesoporous silica: influence of the mesostructured and pore wall properties

Rémi G. Tilkin[a,b], Julien G. Mahy*[a,c], Ana P. F. Monteiro[a,b], Artium Belet[a], Julio Feijóo[a,b], Mathilde Laird[d], Carole Carcel[d], Nicolas Régibeau[a,b], Bart Goderis[e], Christian Grandfils[b], Michel Wong Chi Man[d], Stéphanie D. Lambert[a]*

[a] Department of Chemical Engineering – Nanomaterials, Catalysis and Electrochemistry (NCE), University of Liège, Allée du Six Août 11, 4000 Liège, Belgium

[b] Interfaculty Research Center of Biomaterials (CEIB), University of Liège, Allée du Six Août 11, 4000 Liège, Belgium

[c] Institute of Condensed Matter and Nanosciences (IMCN), Université catholique de Louvain, Place Louis Pasteur 1, 1348, Louvain-la-Neuve, Belgium

[d] ICGM, Univ Montpellier, CNRS, ENSCM, 34095 Montpellier, France

[e] Polymer Chemistry and Materials, KU Leuven, Celestijnenlaan 200F – box 2404, 3001 Heverlee, Belgium

Corresponding authors: Rémi G. Tilkin; email: remitilkin@gmail.com ; address: Allée du Six Août 11, 4000 Liège, Belgium

Julien G. Mahy; email: julien.mahy@uliege.be ; address: Allée du Six Août 11, 4000 Liège, Belgium

ABSTRACT

The goal of this work is to study the influence of the structured mesoporous silica (SMS), used as scaffolds for tissue engineering, on the encapsulation and on the release of a model bone morphogenetic proteins (BMP), *i.e.* Soybean Trypsin Inhibitor (STI).

First, SBA-15 silica samples were synthesized using tetraethyl orthosilicate (TEOS) as silica precursor in the presence of P123 as the surfactant in an acidic medium. Three homemade high-pressure stainless steel reactors (with smaller Teflon reactors inside), each equipped with a temperature probe, were used for the syntheses. In addition, a swelling agent was added to increase the pore size. Indeed, the common pore size for those mesostructured materials lies between 6 nm and 8 nm, while the STI has an average radius of 4 nm. The reagent addition sequence was also investigated, by playing on the time of addition of the swelling agent. It was observed that when the swelling agent was added with TEOS, an ordered mesoporous silica was produced. On the contrary, if the swelling agent was added during the surfactant dissolution step, it resulted in an unstructured yet still mesoporous silica.

Because of the high affinity of STI for hydrophobic surfaces, SMS were also produced using silica precursors containing phenylene bridging groups (*1,4*-bis(triethoxysilyl)benzene, BTEB). The BTEB samples exhibited two 2D-hexagonal structures with different wall thicknesses.

Synthesized materials were further characterized by infrared spectroscopy (FTIR), thermogravimetric analysis (TGA), nitrogen sorption at 77 K, transmission electron microscopy (TEM), and small-angle X-ray scattering (SAXS).

The influence of both the silica composition and structure on STI encapsulation/release was studied. For samples synthesized with TEOS, the unstructured sample showed a higher protein loading and a higher protein release, which could be explained by a difference in the pore interconnectivity within the sample. In fact, a fast release of STI was observed during the first 24

h. Afterwards, the STI release slowed down and seemed to reach a plateau. On the opposite, the structured sample showed a steady release over time. Finally, the sample synthesized with BTEB did not show a significant release over the same period of time. This led us to the conclusion that the hydrophobicity of the silica surface plays a major role on the protein encapsulation and its release rate.

Keywords: biomaterials, bone reconstruction, protein encapsulation, silica gel, sol-gel process, structured silica, ordered mesoporous silica, SBA-15.

1. INTRODUCTION

Bone repair represents a flourishing topic. Every year, over 4 million surgical operations involving bone grafting or bone graft substitutes are performed worldwide [1]. Bone represents the second most grafted organ after blood transfusion

[2]. Moreover, the importance of bone repair is expected to increase continuously in the next decades with the population aging (*i.e.* almost doubling of the population over 65 years in 2050) and the constant increase of need for healthcare worldwide [3].

Several methods have been proposed to recover the complete structure and function of the native bone, including the sustained and local administration of therapeutic biomolecules [4–7]. Among these molecules, bone morphogenetic proteins (BMP), a family of cytokines, have been widely investigated [6–10]. BMP are known to regulate the bone formation via the control of cell adhesion, proliferation, differentiation, and apoptosis. Studies have also demonstrated that the protein BMP-2 could promote the fracture repair by recruiting osteogenic progenitor cells and stimulating the bone differentiation of stem cells [11–13]. Nevertheless, BMP cannot be directly injected into the fracture site because of their rapid clearance [14]. Moreover, an excessively high

dose could lead to an undesirable growth of tumors or neovascularization of non-targeted tissues [15]. Delivery systems with specific textural and chemical properties must therefore be designed to obtain a sustained delivery of BMP [16–18]. In this study, a model protein (*i.e.* Soybean Trypsin Inhibitor, STI) was selected based on its properties (size, molecular weight, point of zero charge, and release kinetics, Table 1), which are similar to the BMP ones [19–21]. Moreover, this protein has been previously used to model BMP release from porous silica [6,20–22].

Table 1 - Properties of STI and BMP-2

Properties	STI	BMP-2
Molecular weight (g/mol)	21,000 [20,22]	26,000 [20]
Size (nm)	4.5 x 4.2 x 4 [23]	7 x 3.5 x 3 [24]
Point of zero charge (pH unit)	4.5 [25]	4.8-5.1 [26]

Structured mesoporous silica (SMS) with well-defined properties (*e.g.* ordered pores, controlled pore size distributions), are attractive to finely tune the loading and the release rate of biopharmaceutical drugs [27–30]. Moreover, thanks to the well-defined periodic geometry of SMS, the protein release can be further regulated by grafting specific responsive molecules, called gates or caps, at the pore opening after loading the biomolecule [31–34]. These gates could indeed prevent the release of the cargo. Once inside the body, the opening of these gates can be triggered by a specific stimulus (*e.g.* a change in pH or in temperature) to release the loaded biomolecules [35–41]. To our knowledge, Ehlert *et al.* are the only ones who have compared the encapsulation of BMP-2 in structured and unstructured silica using an impregnation technique [42]. Surprisingly, the authors have not detected BMP-2 being encapsulated neither in the ordered nor in the disordered silica materials. These observations are therefore in contrast with previously findings published in the literature [6,7,20,22,43,44].

Considering SMS advantages, we envisaged the synthesis of SBA-15 type silica with larger mesopores. In addition to its stability and absence of toxicity, SBA-15 was chosen for its high adsorption capacity [45–49]. The synthesis of SMS was investigated through the use of TEOS as silica precursor [32,50–53]. To obtain larger mesopores than traditional SBA-15, swelling agents such as alcohols, aliphatic/aromatic hydrocarbons are typically added during the synthesis [54–59]. These molecules dissolve inside the hydrophobic part of the micelles, causing a swelling of the later and a subsequent increase in pore size of the final material. Nevertheless, the presence of these additives are known to alter the organization of the material, notably causing a reduction of the degree of organization of the material [46,58]. When using surfactants with a low hydrophilic-lipophilic balance, such as the Pluronic P123, the addition of a swelling agent with low to moderate solubility in water has been recommended to produce SMS combining well-defined structures and large pores [58]. *1,3,5*-triisopropylbenzene (TIPB) is therefore chosen, based on its low water-solubility [46,54,58].

In a second step, based on the high affinity of STI for hydrophobic surfaces [7], SMS were also synthesized with *1,4*-bis(triethoxysilyl)benzene (BTEB). This silica precursor contains a phenylene bridging group between two alkoxysilane moieties (Figure 1), which ensures the regular distribution of these groups within the organosilica walls [60]. The packing of the phenylene groups inside the walls reduces their reactivity and accessibility compared to pendant groups [7,61]. The interactions between the phenylene groups and the protein are therefore weakened thus modulating the STI adsorption strength.

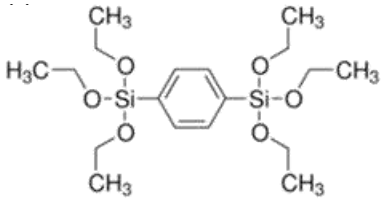

Figure 1 – Chemical structure of BTEB.

The materials were further characterized by infrared spectroscopy (FTIR) to study their chemical composition, thermogravimetric analysis (TGA) to determine the organic content, as well as nitrogen adsorption-desorption at 77 K, transmission electron microscopy (TEM) and small-angle X-ray scattering (SAXS) to assess their textural and morphological properties. The kinetics of STI release were determined over a period of 6 weeks.

2. MATERIALS AND METHODS

2.1. Materials

In this section, the activity of the proteins is expressed in N_{α}-Benzoyl-L-arginine ethyl ester hydrochloride (BAEE) units. One BAEE unit yields a difference in the absorbance at 253 nm (ΔA_{253}) of 0.001/min with BAEE as substrate at pH = 7.6 and at 25 °C.

Tetraethyl orthosilicate (TEOS, $Si(OC_2H_5)_4$) potassium phosphate monobasic (KH_2PO_4), sodium chloride (NaCl), potassium chloride (KCl), *1,2*-dibromoethane, pentane (≥ 95%), *1,4*-dibromobenzene (98 %), deuterochloroform ($CDCl_3$), tetrahydrofuran (THF), and Pluronic P123 were purchased from Sigma-Aldrich; hydrochloric acid (HCl (37 %)), absolute ethanol, and sodium hydroxide (NaOH) were obtained from Merck; ammonium fluoride (NH_4F), sodium phosphate dibasic (Na_2HPO_4), and sodium phosphate monobasic (NaH_2PO_4) were provided by Acros Organics; Soybean Trypsin Inhibitor STI (≥ 7000 BAEE U/mg) was purchased from Carl Roth; *1,3,5*-triisopropylbenzene (TIPB, 95 %) was obtained from Alfa Aesar; Maleic acid

($C_4H_4O_4$) was purchased from Sigma. Unless indicated otherwise, all these chemicals were ≥ 99 % pure and were used without further purification. Phosphate Buffer Saline (PBS) solution was prepared using 1.4 mM KH_2PO_4, 10 mM Na_2HPO_4, 137 mM NaCl and 2.7 mM KCl and was adjusted at *pH* = 7.4 using 0.1 M HCl or 0.1 M NaOH.

2.2. BTEB synthesis

This procedure was adapted from Birault *et al*. [62]. BTEB is prepared by Barbier-Grignard reactions from the respective aryl dibromide and TEOS, as shown in Equation 1.

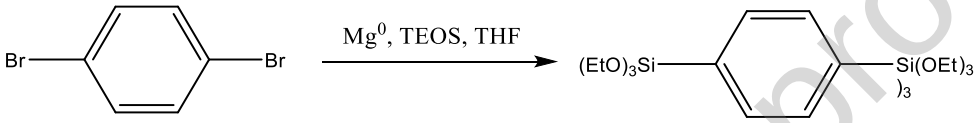

(1)

The reaction was carried out under argon by use of a vacuum line and Schlenk tube techniques. Solvents were dried and distilled before use. To a solution of magnesium turnings (15 g, 0.62 mol) in tetrahydrofuran (THF, 100 mL) placed under argon in a three-neck flask equipped with a magnetic stirrer, a condenser, and an addition funnel, *1,2*-dibromoethane (5 mL) was added dropwise to activate magnesium. When the bubbles from the magnesium activation have stopped, TEOS (450 mL, 2.0 mol) and THF (200 mL) were added. Then, *1,4*-dibromobenzene (48 g, 0.20 mol) dissolved in THF (100 mL) was added dropwise. The temperature was kept below 40 °C using a water bath (exothermic reaction). After stirring at room temperature for 1 h, the THF was evaporated and the resulting solution was filtered over oven-dried celite. The mixture was then extracted with dry pentane. The solvent was evaporated under vacuum. The remaining TEOS was removed by distillation at 86-88 °C under 10^{-1} mbar. The residue was distilled at 125-135 °C under 10^{-1} mbar to obtain BTEB as a pure product. Yield: 51 % ($C_{18}H_{34}O_6Si_2$, 41.1 g, 0.10 mol). ^{1}H NMR (400 MHz, $CDCl_3$, δ, ppm): 7.67 (s, 4 H, Ar*H*), 3.84-3.90 (q, 12 H, O-C*H*$_2$-CH$_3$), 1.21-1.27 (t, 18 H, O-CH$_2$-C*H*$_3$). ^{29}Si NMR (80 MHz, CDCl3, δ, ppm): -58.10.

2.3. Sample preparation

Two silica precursors were used for the synthesis of SMS, *i.e*. TEOS and BTEB. The samples synthesized with TEOS were denoted TEOS-X with X corresponding to the sample number, while the sample produced using BTEB was denoted BTEB.

2.3.1. Synthesis using TEOS as silica precursor

This procedure was adapted from Cao *et al*. [54]. Triblock copolymer Pluronic P123 was selected as template and *1,3,5*-triisopropylbenzene (TIPB) as swelling agent. The synthesis conditions were selected in order to provide a molar ratio TEOS:P123:TIPB:NH_4F:HCl:H_2O of 1:0.0168:0.397:0.0295:4.42:186. Table 2 presents the synthesis conditions of the different silica samples using TEOS as silica precursor. It is important to notice that the TEOS-1, TEOS-2, and TEOS-3 samples come from the same unextracted silica but were treated with different removal treatment techniques.

The syntheses were carried out in homemade high pressure stainless steel reactors (with smaller PTFE reactors inside), thermally regulated with PTFE covered temperature probes plunged into the solution. Those probes were coupled to a double PID controller device, allowing the temperature of individual ovens embedding each reactor to be regulated, thus giving the exact desired temperature inside. For the TEOS-1, TEOS-2, and TEOS-3 samples, P123 and were dissolved in a HCl solution (1.3 M). The solution was poured in the reactor and was firstly stirred at 18 °C for 24 h. A solution of TIPB and TEOS was then added dropwise to the mixture before another subsequent stirring at 18 °C for 24 h. Without opening the reactors, solutions underwent directly the hydrothermal step, consisting in a heating at 100 °C for 48 h, still under moderate stirring. For the TEOS-4 sample, the methodology was the same except that TIPB was not added during the TEOS addition but during the dissolution of P123 and NH_4F. After synthesis, the materials were recovered by centrifugation, washed with deionized water, and dried at 80 °C

under vacuum for 12 h. Surfactant removal was performed via calcination or acidic treatment. For calcination, the samples were heated up to 550 °C at a rate of 1 °C/min for 6 h, under an air flux. For the acidic treatment, untreated silica (0.5 g) was placed in a solution containing ethanol (143 mL) and HCl (4.3 mL, 37 %) for 72 h under reflux. The materials were recovered by centrifugation, washed with ethanol, and dried at 80 °C under vacuum for 24 h. This treatment was applied once for the TEOS-2 sample and twice for the TEOS-3 sample.

Table 2 – Synthesis conditions of the samples synthesized using TEOS.

Sample	Removal treatment	TIPB addition during
TEOS-1	Calcination	TEOS addition
TEOS-2	Acidic x1	TEOS addition
TEOS-3	Acidic x2	TEOS addition
TEOS-4	Calcination	P123 and NH_4F dissolution

2.3.2. Synthesis using BTEB as silica precursor

This procedure was adapted from Laird *et al*. [63]. Triblock copolymer Pluronic P123 was selected as template. The synthesis conditions were selected in order to provide a molar ratio BTEB:P123:HCl:H_2O of 1:0.034:0.462:402.

P123 (1.47 g) was dissolved in deionized water (53.6 mL) at 35 °C. HCl (310 µL, 37 %) was added and the resulting mixture was cooled to 0 °C. BTEB (1.5 g) was then added dropwise and the solution was stirred at 0 °C for 1 h. The solution was then heated to 35 °C for 24 h and then to 100 °C for 24 h under continuous stirring. The material was recovered by centrifugation and washed with deionized water. Surfactant was removed via acidic treatment. The hybrid silica (0.5 g) was extracted in a solution containing HCl (4.3 mL, 37 %) in ethanol (143 mL) for 72 h under reflux. The silica material was recovered by centrifugation, washed with ethanol, and dried at 80 °C under vacuum for 24 h.

2.3.3. Protein encapsulation

The proteins were encapsulated via an impregnation method (performed in triplicates). The samples were impregnated in a STI solution (1 mg/mL in phosphate buffer saline, PBS: 1.4 mM KH_2PO_4, 10 mM Na_2HPO_4, 137 mM NaCl, and 2.7 mM KCl, pH = 7.4) for 72 h at 25 °C under stirring (20 mg of sample per mL of solution). The suspensions were then centrifuged at 10,000 rpm for 5 min and the supernatant was removed. The particles were finally freeze-dried for 72 h.

2.4. Sample characterization

2.4.1. Physicochemical characterization

The purity of the synthesized organosilane was assessed by nuclear magnetic resonance (NMR). Liquid ^{1}H and ^{29}Si NMR spectra were recorded on a Bruker Avance 400 MHz spectrometer in $CDCl_3$ at room temperature and at concentrations of around 1 and 10 mg/mL respectively. All ^{29}Si NMR spectra were proton decoupled.

The physicochemical characterization of the TEOS and BTEB samples was performed on the samples before protein encapsulation.

The presence of specific functional groups was confirmed by Fourier transformed infrared (FTIR) spectroscopy in ATR mode using an IRAffinity-1 from Shimadzu. The following instrumental settings were used: absorbance, range from 4000 to 400 cm^{-1}, 30 scans, resolution of 2 cm^{-1}. The spectra were normalized to the peak corresponding to Si-O-Si stretching (around 1050-1060 cm^{-1}).

The organic content was determined by thermogravimetric analysis (TGA, TGA 7 from Perkin-Elmer) in platinum crucibles under air atmosphere (flow rate of 58 cm^3/min) with a heating rate of 20 °C/min from 50 °C to 90 °C and 10 °C/min from 90 °C to 900 °C. The weight loss fraction *w* (*i.e.* weight loss (g) divided by the sample weight (g)) was measured between 150 °C and 900 °C.

The surface concentration of –OH groups (α_{OH}, -OH group/nm^2) was calculated via Equation 2

$$\alpha_{OH} = 2 \times w \times (1/MM_{H_2O}) \times (1/10^{18}) \times (1/S_{BET}) \times N_A \quad (2)$$

where w is the weight loss fraction (-), MM_{H2O} is the molar mass of water (18.02 g/mol), S_{BET} is the specific surface area evaluated using Brunauer, Emmett, and Teller theory (m²/g), and N_A is the Avogadro's number (6.022 x 10^{23} particle/mol).

The textural and morphological properties were characterized by nitrogen adsorption-desorption isotherms at 77 K in an ASAP 2420 multi-sampler adsorption-desorption volumetric device from Micromeritics. From these isotherms, the total pore volume (V_P) was defined as the specific liquid volume adsorbed at the saturation pressure of nitrogen, the specific surface area was evaluated using Brunauer, Emmett, and Teller theory (S_{BET}), and the mesoporous size distribution was determined by Barrett, Joyner, and Halenda theory (d_{BJH}) [64,65]. The specific mesoporous volume (V_{meso}) and the specific microporous volume (V_{micro}) were evaluated via the t-plot analysis (Figure S2) as fully detailed by Galarneau *et al.* [66].

The textural properties were also studied by small-angle X-ray scattering (SAXS) using a XeuSS setup form Xenocs. The X-ray source was a molybdenum anode, delivering a high-energy monochromatic beam (λ = 0.7107 Å) and providing structural information over scattering vectors q (with $q = (4\pi sin\theta)/\lambda$ and θ being half the scattering angle) ranging from 0.02 to 2.3 Å^{-1}. Only the range $0.02 < q < 0.2$ Å^{-1} was ultimately considered for analysis. The flight tube between sample and the MAR345 image plate detector was purged with helium to avoid air scattering. The data acquisition time was set to 1800 s. The samples were placed in closed aluminum DSC pan. A conversion from the MAR detector data file format to a 16 bits .tiff file was made using FIT2D free software from ESRF (France). An azimuthal averaging, taking into account the sample-detector distance and detector tilting angle, was performed via the free Matlab ConeX

software, developed by Gommes and Goderis [67], and using silver behenate as a calibration standard. Background scattering, based on measuring an empty DSC pan, was subtracted taking into account the individual transmission of each sample. The lattice parameter (a_{SAXS}, Å) was determined as an average of unit-cell parameters defined for the (100), (110) and (200) reflections according to Equations 3, 4, and 5, related to a 2D-hexagonal honeycomb structure

$$a_{100} = 4\pi/(\sqrt{3} \times q_{100}) \quad (3)$$

$$a_{110} = 4\pi/q_{110} \quad (4)$$

$$a_{200} = 8\pi/(\sqrt{3} \times q_{200}) \quad (5)$$

where a_{xxx} is the lattice parameter corresponding to the (xxx) reflection (Å) and q_{xxx} is the scattering vector corresponding to the (xxx) reflection (Å $^{-1}$) [68]. The wall thickness was determined via Equation 6 [69]. It is important to notice that, as the pore are cylindrical, the wall thickness is not constant and that the value determined here is an average value.

$$t = a - 0.95 \times d_{BJH} \quad (6)$$

The textural properties were finally assessed via transmission electron microscopy (TEM). The samples were embedded in epoxy resin SPI-PON 812 (hard mixture, SPI-CHEM, 02659-AB) and left to polymerize for 3 days at 60 °C. Ultrathin sections (thickness = 70-80 nm) were obtained using a diamond knife on an ultramicrotome Reichert Ultracut E and observed in a TEM/STEM Tecnai G2 twin working at 200 kV accelerating voltage and spotsize 3. The lattice parameter (a_{TEM}), the Fast-Fourier transform (FFT) analyses of selected regions of the TEM images, and the size of the elementary particles of the unstructured sample were obtained using ImageJ software (Version 1.53a). The wall thickness was determined via Equation 6.

2.4.2. Biochemical characterization

Protein loading within silica was evaluated by measuring the STI concentration remaining in the supernatant after 72 h of incubation via the Lowry method using STI as a standard (absorbance measurement at 750 nm, spectrophotometer Lambda 25 from Perkin Elmer) [70].

The kinetics of protein release was determined by immersing 20 mg of sample in 1 mL of maleic acid buffer (100 mmol/L, pH = 7.4) in closed vials. This analysis was performed in triplicates. Materials were incubated at 37 °C under continuous agitation. At scheduled times (*i.e.* 30 min, 3 h, 6 h, 1 day, 2 days, 3 days, 1 week, 2 weeks, 4 weeks, 6 weeks), the samples were centrifuged at 10,000 rpm for 5 min. The supernatant was removed, stored at 4 °C until analysis, and replaced by fresh maleic acid buffer. The STI concentration was assessed via the Lowry method using STI as standard (absorbance measurement at 750 nm, spectrophotometer Lambda 25 from Perkin Elmer) [70].

3. RESULTS AND DISCUSSION

3.1. Chemical composition

The effect of the surfactant removal treatment is investigated through two processes: calcination and acidic treatment. Calcination is performed to burn out the surfactant [71,72]. This technique is simpler and faster than other techniques and can be easily implemented at an industrial scale. Moreover, this procedure allows the total removal of residual solvent or unreacted species. Unfortunately, this approach sometimes leads to a considerable shrinkage of the pores and thus a decrease in the pore size. For obvious reasons, the calcination is not suitable in the case of silica containing organic compounds, as it would damage the organic moieties. To tackle these problems, acidic treatment is a suitable alternative. Indeed, it consists in stirring the material in an ethanol solution containing hydrochloric acid at 80 °C for 3-5 days [72–74]. Acidic treatment has been widely used despite its longer processing time compared to calcination because it allows to

maintain the integrity of the pore size distribution while efficiently removing the surfactant molecules. This strategy prevents the pore shrinkage phenomenon associated with calcination. Being performed at a lower temperature (typically below 100 °C), acidic treatment can also be applied to silica containing organic fragments, as the latter are not degraded during the process.

The FTIR absorption spectra of the TEOS samples are displayed in Figure 2 (a-c). Due to the similarities between the spectra of the TEOS-1 and TEOS-4 samples, only the spectrum of the TEOS-1 sample is presented. All FTIR spectra are available in Supplementary Materials, Figure S1. The four FTIR spectra exhibit the characteristic peaks of silica. The peaks corresponding to the bending of Si-O-Si groups are observed at 440-443 cm^{-1} [75–77]. The stretching of Si-O-Si groups is detected at 796 and 811 cm^{-1} (*i.e.* symmetric stretching), at 1057-1067 cm^{-1} (*i.e.* transversal optic mode of asymmetric stretching), and in the 1110-1300 cm^{-1} (*i.e.* longitudinal optic mode of asymmetric stretching) [76–79]. Characteristics peaks of silanol groups are found in the region 540-560 cm^{-1} (*i.e.* rocking mode of Si-OH groups) and around 950-985 cm^{-1} (*i.e.* asymmetric stretching of Si-OH groups) [75,77–79]. These bands are weaker in the case of the calcined sample compared to the untreated sample and the sample after acidic treatment. This can be explained by the condensation of adjacent silanol groups into siloxane bonds during the calcination [80,81]. The difference in intensity observed for the peaks corresponding to –OH groups (*i.e.* bending at 1630 cm^{-1} and stretching around 2800-3700 cm^{-1}) follows the same explanation [75–78,82]. This difference is also explained by the desorption of residual water during the calcination process. Peaks corresponding to the surfactant are observed for the untreated sample, *i.e.* C–H bond (*i.e.* bending at 1345 cm^{-1} and 1450 cm^{-1}), $–CH_2$ groups (*i.e.* bending at 1345 cm^{-1} and 1450 cm^{-1} and stretching around 2880 cm-1 and at 2935 cm^{-1}), $–CH_3$ groups (*i.e.* bending at 1375 cm^{-1}, and stretching around 2880 cm^{-1} and at 2970 cm^{-1}) [78,83,84]. The intensity of these peaks greatly decreases after the first acidic treatment (*i.e.* 4.9-fold

decrease in the area under the curve compared to the untreated sample). These peaks are nevertheless still detected, suggesting the presence of residual surfactant in the pores. In order to reduce the quantity of residual surfactant, a second acidic treatment is performed. This process further decreases the intensity of the peaks (*i.e.* 10.4-fold decrease in the area under the curve compared to the untreated sample) but does not completely remove the surfactant. On the contrary, after calcination, these peaks totally disappear, indicating that surfactant is not present in the pores anymore.

The efficiency of the surfactant removal technique is also determined by TGA (Figure 2 (d)). All samples exhibit similar TGA curves with three consecutive weight losses. The weight loss between 30 and 150 °C (*i.e.* 3-8 wt.%) is assigned to the removal of adsorbed water [63]. Between 150 and 320-350 °C, a second weight loss (*i.e.* 23 wt.% for the untreated sample, 4 wt.% after one acidic treatment, 2 wt.% after two acidic treatment, and < 1 wt.% after calcination) is due to the degradation of residual surfactant in the pores. These results confirm the ones obtained from the FTIR analysis. Indeed, the surfactant content greatly decreases after the acidic treatment (*i.e.* 6.2 and 10.5-fold decrease after one and two acidic treatments respectively, which is similar to the decrease in area under the curve observed in the FTIR analysis) but residual surfactant remains inside the pores. On the opposite, no weight loss is detected between 150 and 350 °C for the sample after calcination, indicating the absence of surfactant. The last weight loss (*i.e.* between 320-350 and 900 °C) corresponds to the condensation of adjacent silanols into siloxane bonds and therefore to the presence of –OH groups. As already mentioned, the lower proportion of –OH groups in the calcined sample (*i.e.* 2 wt.%) compared to the untreated one and the ones treated with acid (*i.e.* 5 wt.%), can be explained by the condensation of adjacent silanols into siloxane bonds during the calcination at 550 °C [80,81]. These values correspond to a surface concentration of –OH groups of 5.2, 3.5, 5.6, and 6.4 –OH groups/nm²

for the sample before treatment, TEOS-1, TEOS-2, TEOS-3, and TEOS-4 respectively, which is in agreement with those obtained by Zhuravlev *et al*. [85].

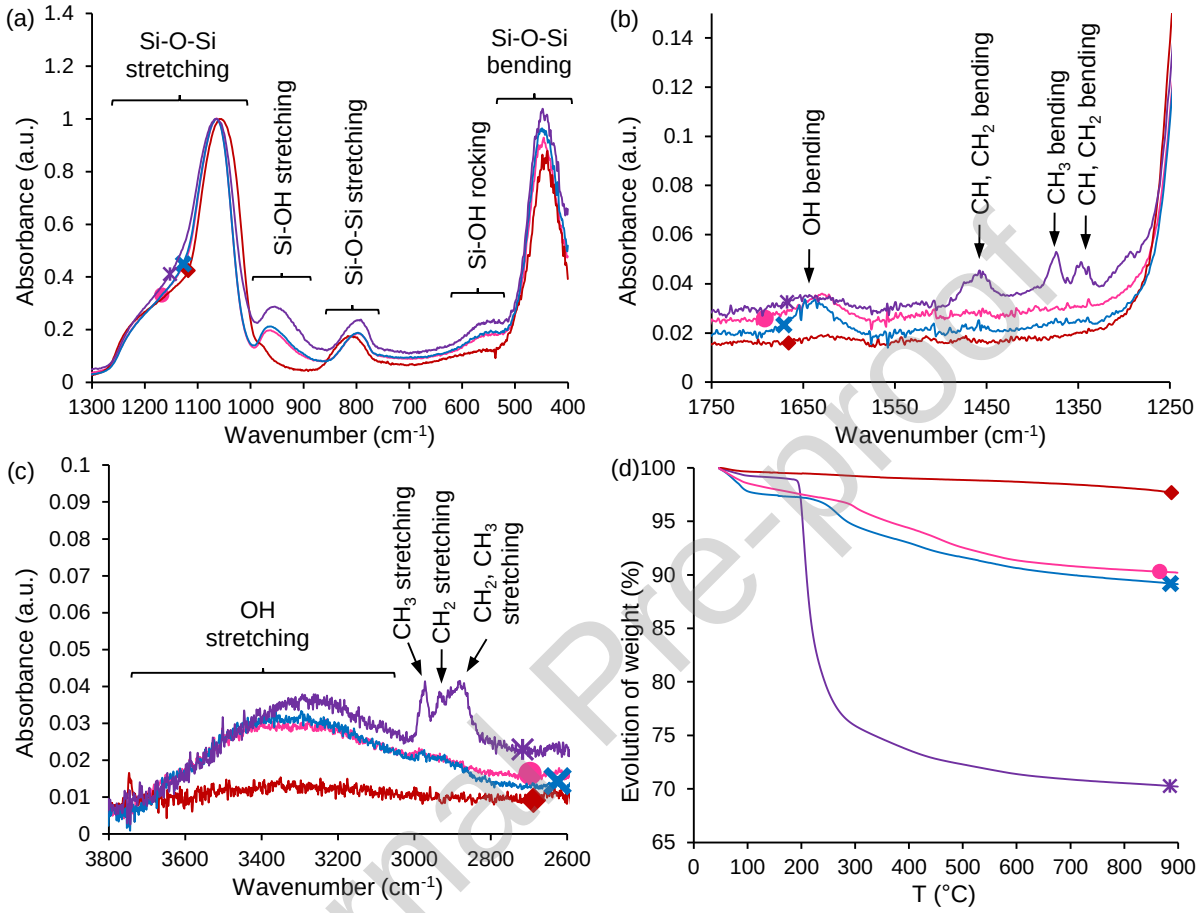

Figure 2 – (a-c) FTIR spectra: (a) zone 400-1300 cm^{-1}, (b) zone 1250-1750 cm^{-1}, (c) zone 2600-3800 cm^{-1} ; and (d) TGA curves of the TEOS samples: ✳ before treatment, ◆ after calcination (TEOS-1), ✕ after the first acidic treatment (TEOS-2), ● after the second acidic treatment (TEOS-3).

The FTIR absorption spectrum of the BTEB sample is displayed in Figure 3 (a-c). The FTIR spectrum exhibits characteristic peaks of silica. Interestingly, these values are shifted towards lower wavenumbers compared to the TEOS samples. The peaks corresponding to the bending of Si-O-Si groups are observed below 400 cm^{-1} [75–77]. The stretching of Si-O-Si groups is detected at 775 cm^{-1} (*i.e*. symmetric stretching), at 1040-1045 cm^{-1} (*i.e*. transversal optic mode of asymmetric stretching), and in the 1090-1200 cm^{-1} (*i.e*. longitudinal optic mode of asymmetric

stretching) [76–79]. Characteristics peaks of silanol groups are found at 520 cm^{-1} (*i.e.* rocking mode of Si-OH groups) and around 915 cm^{-1} (*i.e.* asymmetric stretching of Si-OH groups) [75,77–79]. The shift towards lower wavenumbers is related to the deformation of the network to incorporate the organic groups within the silica matrix (*i.e.* greater Si-O-Si angles and Si-O bond lengths) [78]. The phenyl moieties are detected through the –CH groups (*i.e.* bending around 630, 645, 808, 860, 1152, 1300, and 1380 cm^{-1} and stretching at 3060 cm^{-1}), the aromatic ring (*i.e.* torsion around 630-645 and 1020 cm^{-1}), and –C=C– groups (*i.e.* stretching at 1455 cm^{-1}) [78,83,84,86–88]. The peak at 1205 cm^{-1} can be attributed to the Si-C bond [78]. –OH groups are also found (*i.e.* bending around 1635 cm^{-1} and stretching around 2700-3700 cm^{-1}) [75–78,82].

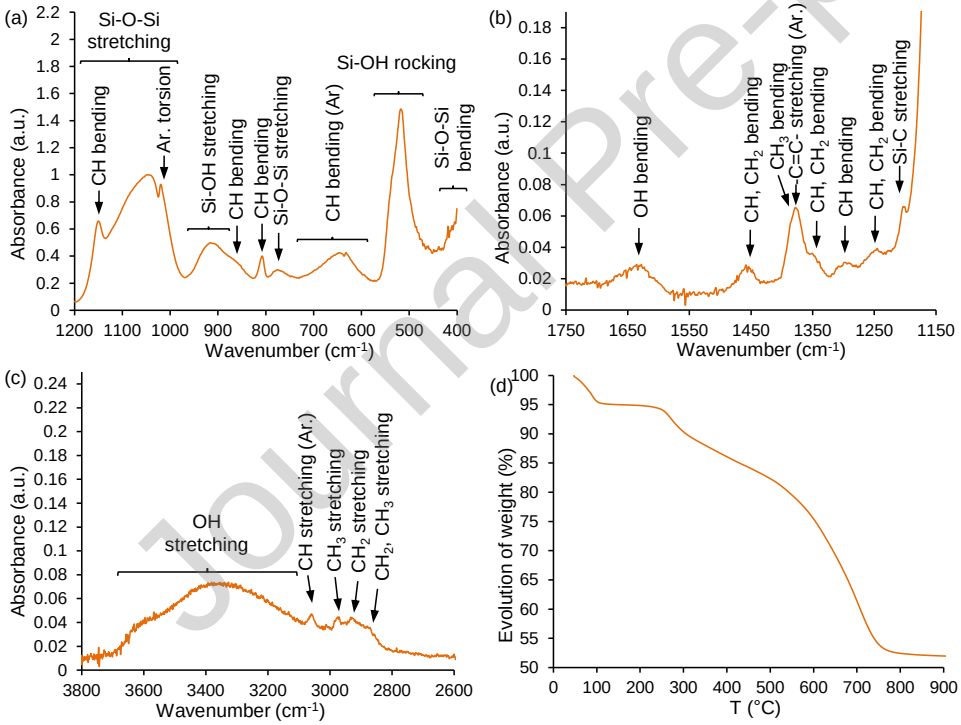

Figure 3 – (a-c) FTIR spectrum: (a) zone 400-1200 cm^{-1}, (b) zone 1150-1750 cm^{-1}, (c) zone 2600-3800 cm^{-1} and (d) TGA curve of the BTEB sample. Ar = Aromatic ring.

As for the TEOS samples, the TGA curve of the BTEB sample present a weight loss between 30 and 150 °C (*i.e.* 8 wt.%) attributed to the removal of water (Figure 3 (d)) [63]. Between 150 and 350 °C, a second weight loss (*i.e.* 7 wt.%) is observed probably due to the degradation of residual

surfactant or unreacted silica precursor (ethoxy groups) in the pores, as it occurs in the same temperature range as for the TEOS samples. This observation explains the presence of peaks corresponding to $–CH_2$ (*i.e.* bending at 1240, 1347, and 1454 cm^{-1} and stretching at 2868 and 2930 cm^{-1}) and $–CH_3$ groups (*i.e.* bending at 1347 cm^{-1} and stretching at 2868 and 2977 cm^{-1}) in the FTIR spectrum of the BTEB sample. The third weight loss (*i.e.* between 350 and 500 °C, 4 wt.%) corresponds to the condensation of adjacent silanols into siloxane bonds and therefore to the presence of –OH groups [89]. This temperature range also corresponds to the degradation of hydrocarbons [90–92]. It can therefore be assumed that the degradation of the structure is also initiated at these temperatures through the oxidation of the phenylene groups present in the sample walls. Above 500 °C, the degraded organic species decompose, leading to the last weight loss (*i.e.* 31 wt.%). The measured proportion of phenylene groups in the materials is obtained by disregarding the weight losses corresponding to the water and the surfactant, *i.e.* by considering that 100 wt.% of the pure materials is present at 350 °C. Based on this assumption, the proportion of phenylene groups is equivalent to 42 wt.%, which is close to the theoretical calculated value (*i.e.* 45.8 wt.%).

In the present application, the presence of residual surfactant would not be a concern. Indeed, Poloxamers are accepted by the US Food and Drug Administration [93,94]. Due to their biocompatibility, Pluronic P-123 has been notably used as a drug delivery vehicle (*e.g.* calcein, curcumin) [95–97].

3.2. Textural properties

The nitrogen adsorption-desorption isotherms are depicted in Figure 4, while the textural properties of the samples are given in Table 3. For all samples, a Type IV isotherms according to the IUPAC classification is present, indicating the presence of micro- and mesopores [98]. Type IV isotherms are characterized by the presence of a hysteresis resulting from capillary condensation occurring inside the mesopores of the material. Two types of hysteresis loops are observed. On the one hand, the Type H1 hysteresis found for the TEOS-1, TEOS-2, and BTEB samples is characterized by hysteresis loop with steep and parallel adsorption/desorption branches, indicating the presence of a narrow range of uniform mesopore sizes. The presence of a large proportion of mesoporous pores is confirmed by the high value of the mesoporous volume compared to the microporous one (Table 3). A shift of the hysteresis towards lower pressure is observed from the TEOS-1 sample to the BTEB one, indicating a lower pore size for the BTEB sample (*i.e.* from 9.8 nm for the TEOS-1 and TEOS-2 samples to 5.1 nm for the BTEB one). When comparing the TEOS-1 and TEOS-2 samples, it is observed that the presence of residual surfactant inside the silica pores does not significantly influence the textural properties of the sample, as both samples exhibit similar isotherms and pore size distributions. The slight difference in specific surface area value (*i.e.* 585 m^2/g for the TEOS-1 sample vs 505 m/g for the TEOS-2 one) between these two samples could be explained by the fact that the residual surfactant trapped inside the pores. Due to the slight difference in textural properties between the sample after the acidic treatment and the calcination, it was decided to not further explore the TEOS-3 sample.

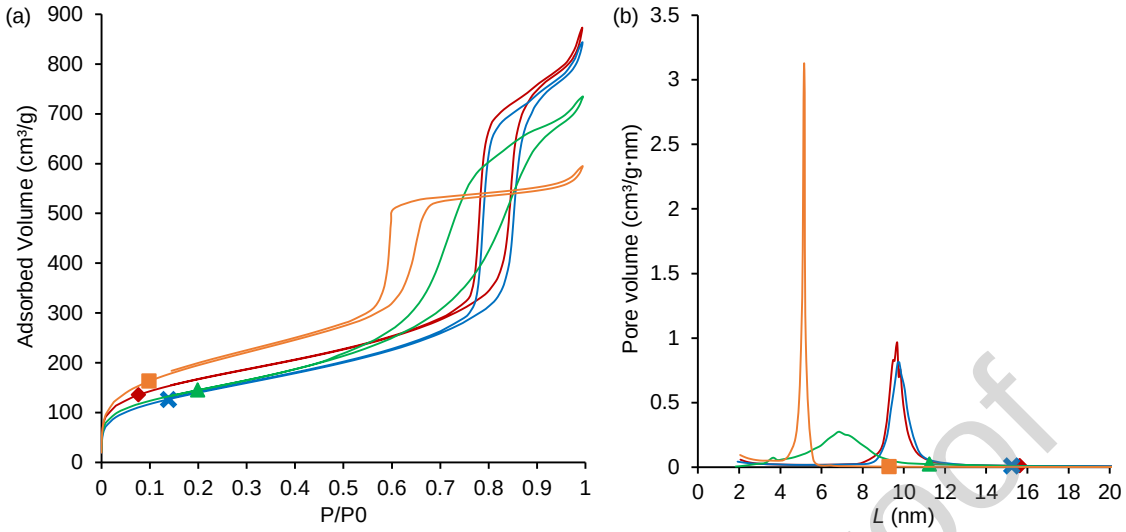

Figure 4 – Nitrogen adsorption-desorption analysis of the TEOS and BTEB samples. (a) Adsorption-desorption isotherms and (b) pore size distributions: ◆ TEOS-1, ✕ TEOS-2, ▲ TEOS-4, ■ BTEB.

On the other hand, the shape of the hysteresis of the TEOS-4 sample (*i.e.* Type H2) points out the presence of disorganized mesopores, suggesting the presence of porous but unstructured silica. This observation shows that the time of TIPB addition greatly affects the textural properties, with the presence of structured silica for the TEOS-1 sample (*i.e.* addition of TIPB during TEOS addition) and unstructured silica for the TEOS-4 sample (*i.e.* addition of TIPB during P123 and NH_4F dissolution). This observation is confirmed by the pore size distribution with a narrow distribution for the TEOS-1 sample (*i.e.* centered at 9.8 nm) compared to a wider pore size distribution for the TEOS-4 sample, going from 3 nm to 12 nm (Figure 4 (b)).

These differences in structure are probably due to the silica network formation mechanism. Without the presence of a swelling agent as TIPB at the beginning of the synthesis, spherical micelles and hydrolyzed TEOS are allowed to interact and their interaction progressively form cylindrical micelles (at the given experimental conditions) where the core is more hydrophobic and the cylindrical surface is more hydrophilic [99,100]. Hydrolyzed TEOS can therefore condense via sol-gel reactions into a silica network around this hydrophilic cylindrical surface.

These micellar aggregates then grow via the incorporation of more silica precursor into the network. As silica is incorporated, micelles associate and form particles, eventually leading to a 2D-hexagonal structure. When TIPB and TEOS are added simultaneously and gradually (dropwise addition), TEOS is rapidly hydrolyzed (acid catalysis and high content in water), which allows its direct association with the spherical micelles. The TEOS precursor then plays a stabilization role of the micelle while the TIPB is added in increasing quantity. The expansion of the micelle is concomitant to the stabilization with the hydrolyzed TEOS thus preserving the 2D-hexagonal structure but with larger pores. By contrast, when added during the dissolution of P123 step, a large quantity of TIPB is allowed to interact with the hydrophobic part of P123 (without stabilization effect of the TEOS), and may prevent the formation of the spherical initiating micelles. In this case, the later addition of TEOS does not trigger the organization of the mesophase, which leads to the condensation of TEOS without soft templating. A disordered silica material is formed.

We could also hypothesize that, in the case of the TEOS-4 sample, the addition of TEOS long time after the addition of the swelling agent leads to micelle structure rearrangement at a time scale comparable to TEOS hydrolysis and condensation, which does not allow for attaining any well-defined structure.

Table 3 – Textural properties of the samples.

Sample	S_{BET} (m^2/g) ± 5	V_P (cm^3/g) ± 0.1	V_{micro} (cm^3/g) ± 0.01	V_{meso} (cm^3/g) ± 0.01	d_{BJH} (nm)
TEOS-1	585	1.3	0.16	1.14	9.8
TEOS-2	505	1.3	0.16	1.14	9.8
TEOS-4	515	1.1	0.10	1.00	6.8
BTEB	700	0.9	0.07	0.83	5.1

Note: S_{BET}: specific surface area determined by the BET method; V_P: specific liquid volume adsorbed at the saturation pressure of nitrogen; V_{micro}: specific microporous volume determined by t-plot analysis; V_{meso}: specific mesoporous volume determined by t-plot analysis; d_{BJH}: mean pore size determined by the BJH theory.

The SAXS patterns of the structured samples (*i.e.* TEOS-1, TEOS-2, and BTEB samples) are illustrated in Figure 5. The pattern of the TEOS-1 and TEOS-2 samples exhibits five pseudo-Bragg peaks in the low q region with q_0 equal to 4.9 x 10^{-2} and 4.6 x 10^{-2} $Å^{-1}$ respectively. The relative position of the peaks corresponds to the (100), (110), (200), (210), and (300) reflections from a 2D-hexagonal mesostructure ($P6_3/m$ symmetry) with a lattice parameter a_{SAXS} equal to 14.8 nm for the TEOS-1 sample and to 15.5 nm for the TEOS-2 one [54,63]. The fact that the (210) and (300) reflections can be seen shows that the silica is highly organized. By contrast, the SAXS pattern of the BTEB sample exhibits two sets of peaks. The first set (q_0 equal to 7.2 x 10^{-2} $Å^{-1}$, indicated with the symbol #) corresponds to the (100), (110), and (200) reflections from a 2D-hexagonal structure with a lattice parameter a_{SAXS} = 10.1 nm. The second set (q_0 equal to 8.6 x 10^{-2} $Å^{-1}$, indicated with a symbol *) corresponds to the (100), (110), and (200) reflections from a 2D-hexagonal structure with a smaller lattice parameter, *i.e.* a_{SAXS} = 8.6 nm. In contrast to these structured silica samples, the TEOS-4 sample (Figure S4 available in Supplementary Materials) does not present a pseudo-Bragg peaks, indicating the absence of organization in this sample.

The TEM analysis corroborates the nitrogen adsorption-desorption and SAXS measurements (Figure 6, Table 4). The TEOS-1 and TEOS-2 samples exhibit an organized porosity with

hexagonal symmetry, as shown by the honeycomb structures observed. The corresponding FFT data (inserts in Figure 6, larger representation is available in Supplementary Materials, Figure S3) are consistent with hexagonal symmetry, as characteristic hexagonal features are observed. The apparent wall thickness, calculated from the lattice parameter a_{TEM} and the pore diameter determined via nitrogen adsorption, d_{BJH}, is similar for the two samples, *i.e.* close to 3.6 nm. A similar honeycomb structure is observed for the BTEB sample, indicating an organized porosity with hexagonal symmetry. Yet, as shown by the superposition of two series of characteristic hexagonal features in the FTT data, it appears that two hexagonal structures with different lattice parameters are present. Taking into account that the BTEB sample only exhibits one pore size, these two structures correspond to two different wall thicknesses. Unfortunately, only one lattice parameter could be found. It is hypothesized that, due to the small difference between the lattice parameter values, the two structures could not be differentiated with the image treatment and that the value obtained is a mean of the two values. In contrast to these structured silica samples, the TEOS-4 sample does not present a honeycomb feature but is rather composed of spherical elementary particles with a size of 30±4 nm.

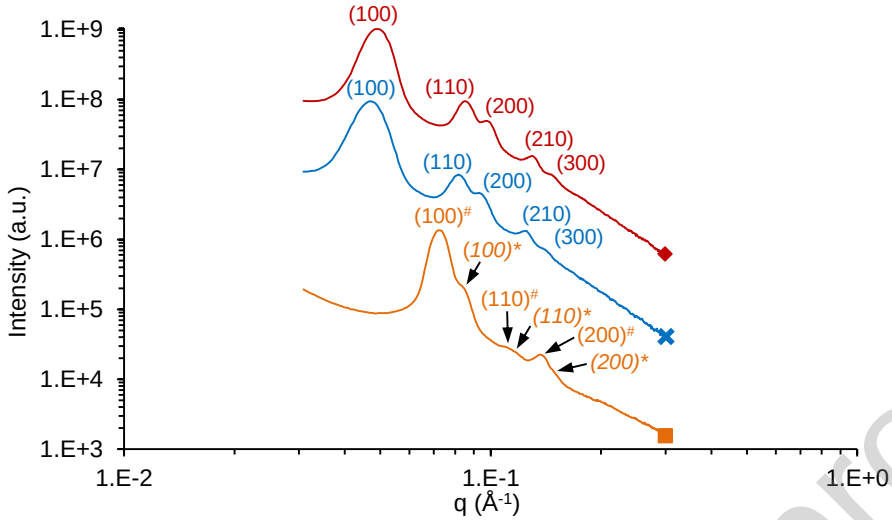

Figure 5 – SAXS analysis of the ◆ TEOS-1, ✕ TEOS-2, ■ BTEB samples. For the BTEB sample, the first set of peaks is indicated with the symbol # and the second one with the symbol *.

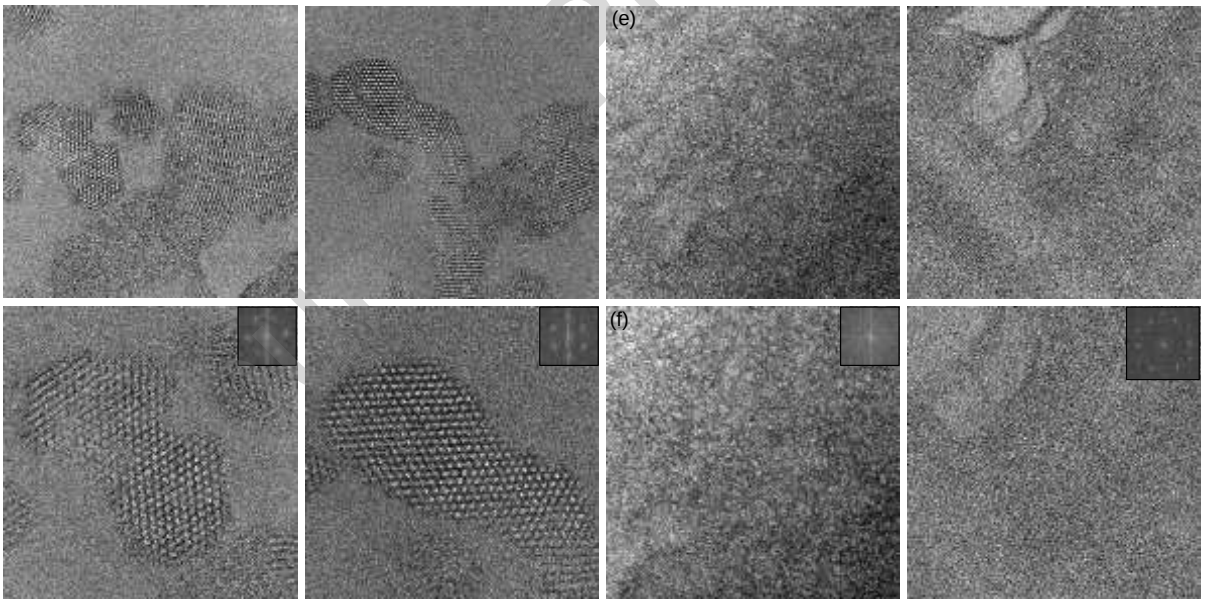

Figure 6 – TEM images of the (a-b) TEOS-1, (c-d) TEOS-2, (e-f) TEOS-4, and (g-h) BTEB samples. The inserts in (b-d-f-h) are the corresponding FFT.

Table 4 – Textural properties of the organized samples (TEM and SAXS analysis).

Sample	TEM analysis		SAXS analysis	
	a_{TEM} (nm)	t_{TEM} (nm)	a_{SAXS} (nm)	t_{SAXS} (nm)
TEOS-1	13.4 ± 0.5	4.1	14.8	5.5
TEOS-2	13.5 ± 1.1	4.2	15.5	6.2
BTEB	9.1 ± 0.4	4.3	8.6-10.1	3.8-5.3

Note: a_{TEM} and t_{TEM}: lattice parameter (pore size + wall size) and wall size determined by TEM; a_{SAXS} and t_{SAXS}: lattice parameter (pore size + wall size) and wall size determined by SAXS.

3.3. Protein encapsulation

The amount of encapsulated STI per unit mass of silica and per unit of specific surface area of silica are presented in Figure 7. The protein is encapsulated on the TEOS-1 and TEOS-4 samples, in order to study the effect of the silica structure on the encapsulation of the protein. It is important to keep in mind that these samples were synthesized using the same synthesis protocol (except for the time of addition of TIPB) and that great care was taken to ensure identical experimental parameters, *i.e.* pH, solvent, temperature and stirring (*cf.* section 2.3.1). The BTEB sample is also considered for the protein encapsulation in order to study the influence of the presence of phenylene groups within the sample walls.

The amount of encapsulated STI greatly varies among samples. A larger protein loading is observed for the unstructured TEOS-4 sample (38 mg/g) when compared to the structured ones (19 mg/g for the TEOS-1 sample and 21 mg/g for the BTEB one), regardless of the silica precursor nature. This can be explained by a blockage of the pores by the proteins [101,102]. Indeed, even if the pore were to be larger than the STI average radius (about 4 nm), the adsorption of two protein molecules on the same pore section would hinder the pore, preventing further protein insertion inside this pore. In the case of ordered silica materials, the blockage of the two extremities of the pore seals the entire pore off, greatly decreasing the surface area

accessible for protein adsorption. On the opposite, unstructured silica (*i.e.* TEOS-4 sample) is composed of an interconnected network of pores. Therefore, if a pore is blocked on one side, the proteins can diffuse through other paths. The amount of adsorbed STI in "per specific surface area" of each sample (Figure 7(b)) follow the same rationale. The values for the TEOS-4 sample are similar to those previously observed for calcined unstructured silica [7].

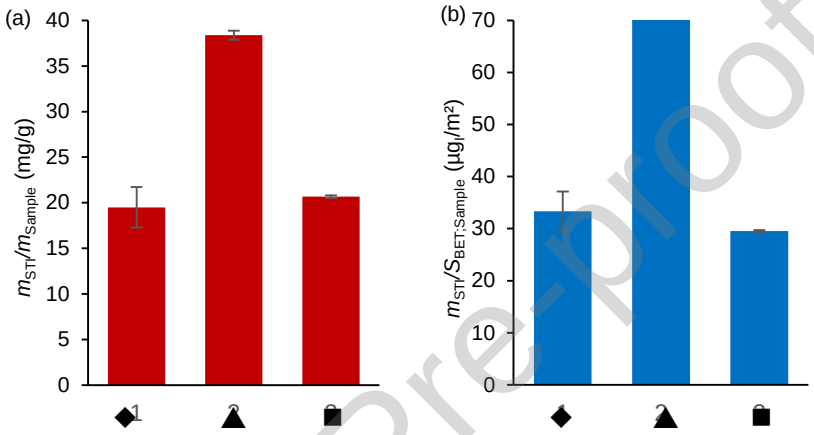

Figure 7 – STI loading expressed as (a) m_{STI}/m_{Sample} and (b) $m_{STI}/S_{BET;Sample}$ in the TEOS and BTEB samples: ◆ TEOS-1, ▲ TEOS-4, ■ BTEB.

It is important to note that these results represent the total amount of protein, i.e. inside and at the external surface of the samples.

3.4. Release kinetics profiles

Figure 8 illustrates the release kinetic profiles. For the sake of clarity, Figure 8 was divided into three parts: (a) profiles over 45 days, (b) zoom on the first 24 h of release, and (c) amount of STI released after the first day. The last subfigure is expressed as the percentage of STI remaining in the silica after day 1, meaning that the amount of STI released up to 24 h was subtracted.

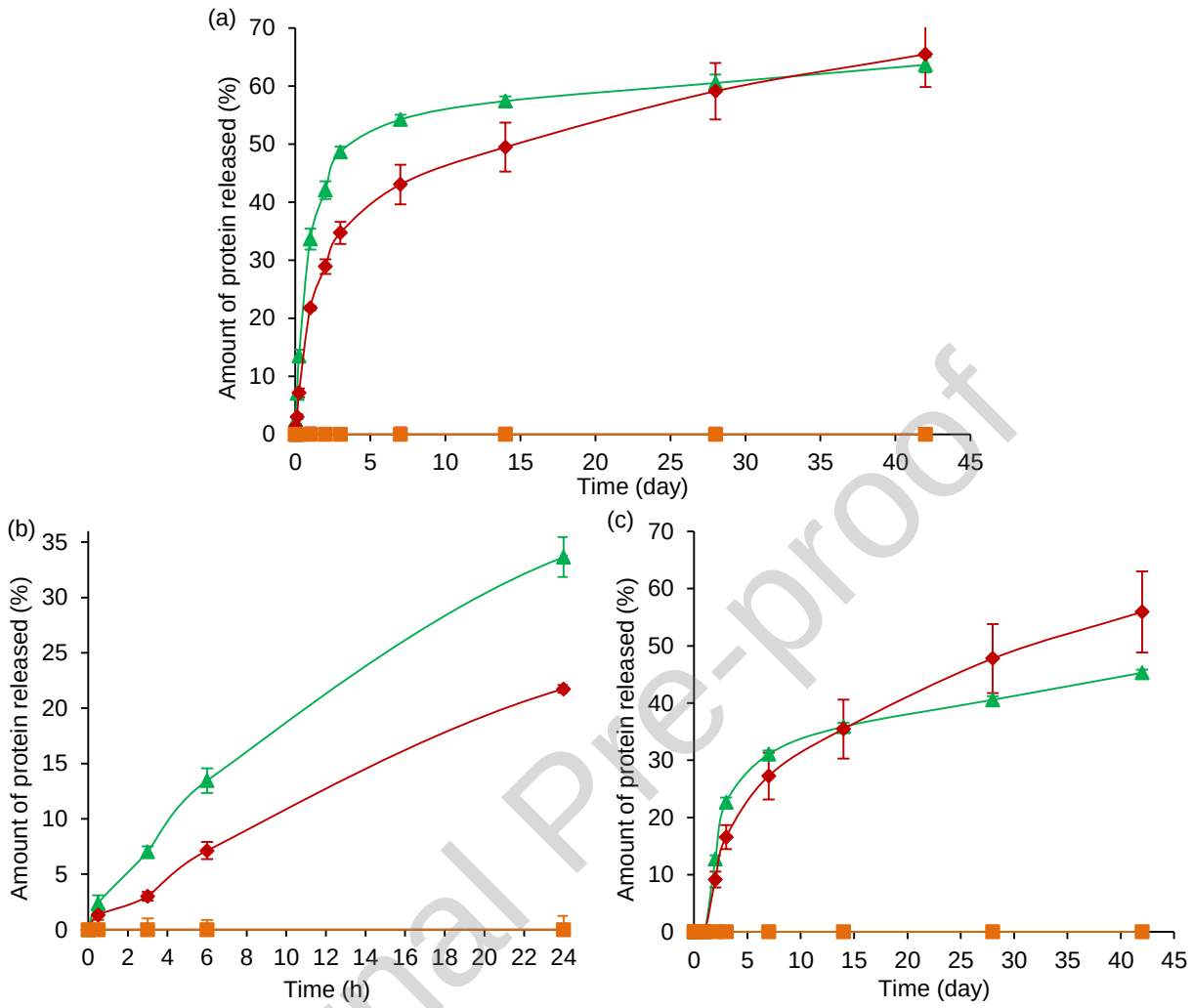

Figure 8 – Release kinetics profile of STI from the TEOS and BTEB materials: (a) Release kinetics profile over 45 days (b) Initial release profile (0 to 24 h) (c) Profile of the STI released after the first day (STI release up to 24 h is subtracted): ◆ TEOS-1, ▲ TEOS-4, ■ BTEB.

Regarding the TEOS samples, the release kinetics profiles highlight a relatively fast release of STI from both samples within the first 24 h. During this period, 20 and 35 % of the encapsulated STI are released from the TEOS-1 and TEOS-4 samples respectively. It is assumed that this premature release is mostly resulting from the liberation of the fraction of the protein adsorbed on the external surface of the silica particles, which can easily and rapidly desorb upon immersion. Considering the results of this section, it seems that the proteins present at the surface of the silica

account for 20 to 35 % of the total amount. This means that the quantity of encapsulated proteins is equal to 15 mg/g for the TEOS-1 sample and to 26 mg/g for the TEOS-4 one.

Assuming that the burst is probably due to STI adsorbed at the surface, we have decided to remove the part corresponding to the premature release in order to focus on the release of the protein encapsulated inside the silica pores. We therefore express the rest of the profile as the proportion of the remaining STI after 24 h that is released in the medium (Figure 8(c)). Beyond this period, the STI release slows down for the TEOS-4 sample. The release profile seems to achieve a plateau, as observed in previous studies [6,7]. The STI retention might be linked to the interactions between the protein and silanol groups present at the surface of the pores, preventing the total release of the protein. By contrast, a sustained release of STI is observed up to day 42 for TEOS-1, as the release profile does not seem to reach a plateau within the studied period. These results indicate that structured silica can produce a sustained release on a longer period than porous unstructured silica. This difference can be explained by the pore interconnectivity [102,103]. In the case of structured silica (*i.e.* TEOS-1 sample), the proteins can only diffuse through the two extremities of a given pore, since the STI size does not allow it to diffuse through micropore channels that connect the mesoporous cylinders together. Therefore, proteins that are adsorbed at the centre of a pore cannot easily diffuse outside as long as there are proteins in their path to the exit. On the opposite, the unstructured sample presents an interconnected network of mesopores. In this case, the proteins can bypass possible pore blockage, as they would have more opportunities of escaping the silica matrix and be released.

In contrast with the TEOS samples, the BTEB sample does not present a significant release of STI over the 30 days period. These observations corroborates the high affinity of the STI for the phenylene groups, as previously shown [7]. It is important to notice that phenylene groups represented a high proportion of the materials (*i.e.* 22 wt.% in [7] and 42 wt.% in this present

study). It is expected that an adequate balance of hydrophobic/hydrophilic groups could enable a tailored release kinetic of the STI protein to be obtained by controlling the hydrophobicity of the material with the BTEB content. This can be envisioned by inserting polar organic groups (such as amino groups) in the pore walls which will surely allow more hydrophilic characteristics and favour the release of STI.

4. CONCLUSIONS

In conclusion, SBA-15 type silica samples were first synthesized using TEOS as silica precursor in the presence of a swelling agent to increase the pore size. Two different surfactant removal treatments were investigated, *i.e.* calcination and acidic treatment. The latter treatment did not completely remove the surfactant, while no trace of residual surfactant was detected in the calcined samples. Yet, the samples produced with these two techniques exhibited similar textural morphological properties as well as 2D-hexagonal honeycomb mesostructures. The reagent addition sequence was also investigated, specifically by playing on the time of addition of a swelling agent (TIPB). The textural analysis showed the presence of organization in the sample for which the swelling agent was added together with the TEOS. On the opposite, when the swelling agent was added during the surfactant dissolution, porous unstructured silica was produced.

Based on the high affinity of STI for hydrophobic surfaces, SMS were also produced using BTEB to incorporate phenylene groups inside the wall matrix. In contrast with the TEOS samples, the BTEB sample exhibited two hexagonal structures with different wall thicknesses, as shown by the TEM and SAXS analyses.

The influence of the silica structure (*i.e.* ordered vs disordered) and composition (*i.e.* TEOS vs BTEB) on STI encapsulation and release was finally studied. The higher protein loading

observed for the unstructured sample (compared to the structured materials regardless of the nature of the silica precursor) was explained by a difference in the pore interconnectivity among the samples. Regarding the release profiles, for the TEOS samples, a fast release of STI was observed during the first 24 h. Beyond this period, the STI release slowed down for the unstructured sample and seemed to reach a plateau, while a sustained release of STI was observed up to day 28 for the structured sample. These results were also explained by a difference in pore interconnectivity thus highlighting the capacity of the ordered silica to release the protein on a more gradual manner. On the opposite, the BTEB sample did not show any significant release of STI over the 30 days period, because of a higher affinity of the protein towards phenylene groups. As perspective, more efforts should be devoted to better adjust the hydrophobicity of the silica surface, in order to optimally reduce the protein binding and enhance its release rate.

5. ACKNOWLEDGMENTS

Funding: This work was supported by the Belgian Fund for Scientific Research (F.R.S.-FNRS) under a Fund for Research Training in Industry and Agriculture (FRIA) grant, the "Ministère wallon de la Recherche et de l'Innovation", and the Wallonia region.

Stéphanie D. Lambert, Julien G. Mahy and Ana P. F. Monteiro thank the F.R.S.-FNRS for their Senior Research Associate position and Postdoctoral Researcher positions respectively. Rémi G. Tilkin and Nicolas Régibeau also thank the F.R.S.-FNRS for their FRIA grant.

The authors thank Dr. Ir. Cedric J. Gommes for his help to process the SAXS data and for fruitful and interesting discussions.

The authors thank Camille Tilkin for her corrections.

6. CONFLICT OF INTEREST

The authors declare that there is no conflict of interest concerning this work.

7. REFERENCES

[1] A.S. Brydone, D. Meek, S. MacLaine, Bone grafting, orthopaedic biomaterials, and the clinical need for bone engineering, Proc. Inst. Mech. Eng. Part H J. Eng. Med. 224 (2010) 1329–1343. doi:10.1243/09544119JEIM770.

[2] V. Campana, G. Milano, E. Pagano, M. Barba, C. Cicione, G. Salonna, W. Lattanzi, G. Logroscino, Bone substitutes in orthopaedic surgery: from basic science to clinical practice, J. Mater. Sci. Mater. Med. 25 (2014) 2445–2461. doi:10.1007/s10856-014-5240-2.

[3] US Census Bureau, Statistical abstracts of the United States: 2012 - Section 1. Population, (2012). www.census.gov/library/publications/2011/compendia/statab/131ed/population.html (accessed November 25, 2019).

[4] S. Bhattacharyya, H. Wang, P. Ducheyne, Polymer-coated mesoporous silica nanoparticles for the controlled release of macromolecules, Acta Biomater. 8 (2012) 3429–3435. doi:10.1016/j.actbio.2012.06.003.

[5] S. Chen, X. Shi, H. Morita, J. Li, N. Ogawa, T. Ikoma, S. Hayakawa, Y. Shirosaki, A. Osaka, N. Hanagata, BMP-2-loaded silica nanotube fibrous meshes for bone generation, Sci. Technol. Adv. Mater. 12 (2011) 065003. doi:10.1088/1468-6996/12/6/065003.

[6] R.G. Tilkin, X. Colle, A. Argento Finol, N. Régibeau, J.G. Mahy, C. Grandfils, S.D.

Lambert, Protein encapsulation in functionalized sol-gel silica : Effect of the encapsulation method on the release kinetics and the activity, Microporous Mesoporous Mater. 308 (2020) 110502. doi:10.1016/j.micromeso.2020.110502.

[7] R.G. Tilkin, J.G. Mahy, N. Régibeau, R. Vandeberg, A.P.F. Monteiro, C. Grandfils, S. Lambert, Protein encapsulation in functionalized sol – gel silica : influence of organosilanes and main silica precursors, J. Mater. Sci. 56 (2021) 14234–14256. doi:10.1007/s10853-021-06182-9.

[8] K.W. Lo, B.D. Ulery, K.M. Ashe, C.T. Laurencin, Studies of bone morphogenetic protein-based surgical repair, Adv. Drug Deliv. Rev. 64 (2012) 1277–1291. doi:10.1016/j.addr.2012.03.014.

[9] C.J. Hwang, A.R. Vaccaro, J.P. Lawrence, J. Hong, H. Schellekens, M.H. Alaoui-Ismaili, D. Falb, Immunogenicity of bone morphogenetic proteins, J. Neurosurg. Spine SPI. 10 (2009) 443–551. doi:10.3171/2009.1.SPINE08473.

[10] P.C. Bessa, M. Casal, R.L. Reis, Bone morphogenetic proteins in tissue engineering: the road from laboratory to clinic , part II (BMP delivery), J. Tissue Eng. Regen. Med. 2 (2008) 81–96. doi:10.1002/term.

[11] Y. Kimura, D. Ph, N. Miyazaki, M. Eng, N. Hayashi, M. Eng, Controlled Release of Bone Morphogenetic Protein-2 Enhances Recruitment of Osteogenic Progenitor Cells for De Novo Generation of Bone Tissue, Tissue Eng. Part A. 16 (2010) 1263–1270. doi:10.1089/ten.tea.2009.0322.

[12] J. Yamashita, B.R. Furman, H.R. Rawls, X. Wang, C.M. Agrawal, The use of dynamic mechanical analysis to assess the viscoelastic properties of human cortical bone., J. Biomed. Mater. Res. 58 (2001) 47–53. doi:10.1002/1097-4636(2001)58:1<47::AID-JBM70>3.0.CO;2-U.

[13] J. Sun, J. Li, C. Li, Y. Yu, Role of bone morphogenetic protein-2 in osteogenic differentiation of mesenchymal stem cells, Mol. Med. Rep. 12 (2015) 4230–4237. doi:10.3892/mmr.2015.3954.

[14] I. El Bialy, W. Jiskoot, M.R. Nejadnik, Formulation, Delivery and Stability of Bone Morphogenetic Proteins for Effective Bone Regeneration, Pharm. Res. 34 (2017) 1152–1170. doi:10.1007/s11095-017-2147-x.

[15] H. Jung, S. Yook, C. Han, T. Jang, H. Kim, Y. Koh, Y. Estrin, Highly aligned porous Ti scaffold coated with bone morphogenetic protein-loaded silica / chitosan hybrid for enhanced bone regeneration, J. Biomed. Mater. Res. Part B Appl. Biomater. 102B (2014) 913–921. doi:10.1002/jbm.b.33072.

[16] J.A. Schrier, P.P. Deluca, Recombinant Human Bone Morphogenetic Protein-2 Binding and Incorporation in PLGA Microsphere Delivery Systems, Pharm. Dev. Technol. 4 (1999) 611–621. doi:10.1081/PDT-100101400.

[17] M.R. Johnson, H. Lee, R. V Bellamkonda, R.E. Guldberg, Sustained release of BMP-2 in a lipid-based microtube vehicle, Acta Biomater. 5 (2009) 23–28. doi:10.1016/j.actbio.2008.09.001.

[18] Y. Li, Y. Song, A. Ma, C. Li, Surface Immobilization of TiO2 Nanotubes with Bone Morphogenetic Protein-2 Synergistically Enhances Initial Preosteoblast Adhesion and Osseointegration, Biomed Res. Int. 2019 (2019) 5697250. doi:10.1155/2019/5697250.

[19] J. Hum, A.R. Boccaccini, Bioactive glasses as carriers for bioactive molecules and therapeutic drugs : a review, J. Mater. Sci. Mater. Med. 23 (2012) 2317–2333. doi:10.1007/s10856-012-4580-z.

[20] T. Reiner, S. Kababya, I. Gotman, Protein incorporation within Ti scaffold for bone ingrowth using Sol-gel SiO2 as a slow release carrier, J. Mater. Sci. Mater. Med. 19 (2008)

583–589. doi:10.1007/s10856-007-3194-3.

[21] C.M. Agrawal, J. Best, J.D. Heckman, B.D. Boyan, Protein release kinetics of a biodegradable implant for fracture, Biomaterials. 16 (1995) 1255–1260. doi:10.1016/0142-9612(95)98133-Y.

[22] E.M. Santos, S. Radin, P. Ducheyne, Sol-gel derived carrier for the controlled release of proteins, Biomaterials. 20 (1999) 1695–1700. doi:10.1016/S0142-9612(99)00066-6.

[23] H.K. Song, S.W. Suh, Kunitz-type Soybean Trypsin Inhibitor Revisited : Refined Structure of its Complex with Porcine Trypsin Reveals an Insight into the Interaction Between a Homologous Inhibitor from Erythrina caffra and Tissue-type Plasminogen Activator, J. Mol. Biol. 275 (1998) 347–363. doi:10.1006/jmbi.1997.1469.

[24] C. Scheufler, W. Sebald, M. Hülsmeyer, Crystal structure of human bone morphogenetic protein-2 at 2.7 Å resolution1, J. Mol. Biol. 287 (1999) 103–115. doi:10.1006/jmbi.1999.2590.

[25] Y. Chang, T.C. Liu, M. Tsai, Selective Isolation of Trypsin Inhibitor and Lectin from Soybean Whey by Chitosan / Tripolyphosphate / Genipin Co-Crosslinked Beads, Int. J. Mol. Sci. 15 (2014) 9979–9990. doi:10.3390/ijms15069979.

[26] J. Yang, P. Shi, M. Tu, Y. Wang, M. Liu, F. Fan, M. Du, Bone morphogenetic proteins: Relationship between molecular structure and their osteogenic activity, Food Sci. Hum. Wellness. 3 (2014) 127–135. doi:10.1016/j.fshw.2014.12.002.

[27] M. Vallet-Regi, A. Ramila, R.P. del Real, J. Perez-Pariente, A New Property of MCM-41 : Drug Delivery System, Chem. Mater. 13 (2001) 308–311. doi:10.1021/cm0011559.

[28] M. Fernanandez-Nunez, D. Zorrilla, A. Montes, M.J. Mosquera, Ibuprofen Loading in Surfactant-Templated Silica : Role of the Solvent According to the Polarizable Continuum Model, J. Phys. Chem. A. 113 (2009) 11367–11375. doi:10.1021/jp903895r.

[29] V. Zelenak, D. Halamová, M. Almáši, L. Zid, A. Zelenáková, O. Kapusta, Applied Surface Science Ordered cubic nanoporous silica support MCM-48 for delivery of poorly soluble drug indomethacin, Appl. Surf. Sci. J. 443 (2018) 525–534. doi:10.1016/j.apsusc.2018.02.260.

[30] A. Szewczyk, M. Prokopowicz, Amino-modified mesoporous silica SBA-15 as bifunctional drug delivery system for cefazolin : Release profile and mineralization potential, Mater. Lett. 227 (2018) 136–140. doi:10.1016/j.matlet.2018.05.059.

[31] H. Mekaru, J. Lu, F. Tamanoi, Development of mesoporous silica-based nanoparticles with controlled release capability for cancer therapy ☆ a) Liposome, Adv. Drug Deliv. Rev. 95 (2015) 40–49. doi:10.1016/j.addr.2015.09.009.

[32] R. Narayan, U.Y. Nayak, A.M. Raichur, S. Garg, Mesoporous Silica Nanoparticles : A Comprehensive Review on Synthesis and Recent Advances, Pharmaceutics. 10 (2018) 1–49. doi:10.3390/pharmaceutics10030118.

[33] S. Wang, Microporous and Mesoporous Materials Ordered mesoporous materials for drug delivery, Microporous Mesoporous Mater. 117 (2009) 1–9. doi:10.1016/j.micromeso.2008.07.002.

[34] T. Ukmar, O. Planinsek, Ordered mesoporous silicates as matrices for controlled release of drugs, Acta Pharm. 60 (2010) 373–385. doi:10.2478/v1007-010-0037-4.

[35] C. Théron, A. Gallud, C. Carcel, M. Gary-Bobo, M. Maynadier, M. Garcia, J. Lu, F. Tamanoi, J.I. Zink, M. Wong Chi Man, Hybrid Mesoporous Silica Nanoparticles with pH-Operated and Complementary H-Bonding Caps as an Autonomous Drug- Delivery System, Nanoparticles. 20 (2014) 9372–9380. doi:10.1002/chem.201402864.

[36] C. Théron, A. Gallud, S. Giret, M. Maynadier, D. Grégoire, P. Puche, E. Jacquet, G. Pop,

O. Sgarbura, V. Bellet, U. Hibner, J.I. Zink, M. Garcia, M. Wong Chi Man, C. Carcel, M. Gary-Bobo, pH-operated hybrid silica nanoparticles with multiple H-bond stoppers for colon cancer therapy, RSC Adv. 5 (2015) 64932–64936. doi:10.1039/C5RA09891B.

[37] S. Song, K. Hidajat, S. Kawi, pH-Controllable drug release using hydrogel encapsulated mesoporous silica, Chem. Commun. (2007) 4396–4398. doi:10.1039/b707626f.

[38] Q. Gan, J. Zhu, Y. Yuan, H. Liu, J. Qian, Y. Li, C. Liu, A dual-delivery system of pH-responsive chitosan-functionalized mesoporous silica nanoparticles bearing BMP-2 and dexamethasone for enhanced bone regeneration, J. Mater. Chem. B. 3 (2015) 2056–2066. doi:10.1039/c4tb01897d.

[39] A. Baeza, E. Guisasola, E. Ruiz-herna, Magnetically Triggered Multidrug Release by Hybrid Mesoporous Silica Nanoparticles, Chem. Mater. 24 (2012) 517–524. doi:10.1021/cm203000u.

[40] Q. Fu, G.V.R. Rao, L.K. Ista, Y. Wu, B.P. Andrzejewski, L.A. Sklar, T.L. Ward, G.P. López, Control of Molecular Transport Through Stimuli-Responsive Ordered Mesoporous Materials, Adv. Mater. 15 (2003) 1262–1266. doi:10.1002/adma.200305165.

[41] E. Yu, A. Lo, L. Jiang, B. Petkus, N.I. Ercan, P. Stroeve, Improved controlled release of protein from expanded-pore mesoporous silica nanoparticles modified with co-functionalized poly(n-isopropylacrylamide) and poly(ethylene glycol) (PNIPAM-PEG), Colloids Surfaces B Biointerfaces. 149 (2017) 297–300. doi:10.1016/j.colsurfb.2016.10.033.

[42] N. Ehlert, A. Hoffmann, T. Luessenhop, G. Gross, P.P. Mueller, M. Stieve, T. Lenarz, P. Behrens, Amino-modified silica surfaces efficiently immobilize bone morphogenetic protein 2 (BMP2) for medical purposes, Acta Biomater. 7 (2011) 1772–1779. doi:10.1016/j.actbio.2010.12.028.

[43] W. Tang, D. Lin, Y. Yu, H. Niu, H. Guo, Y. Yuan, C. Liu, Bioinspired trimodal macro / micro / nano-porous scaffolds loading rhBMP-2 for complete regeneration of critical size bone defect, Acta Biomater. 32 (2016) 309–323. doi:10.1016/j.actbio.2015.12.006.

[44] S.B. Nicoll, S. Radin, E.M. Santos, R.S. Tuan, P. Ducheyne, In vitro release kinetics of biologically active transforming growth factor-β1 from a novel porous glass carrier, Biomaterials. 18 (1997) 853–859. doi:10.1016/S0142-9612(97)00008-2.

[45] H. Tan, S. Yang, P. Dai, W. Li, B. Yue, Preparation and physical characterization of calcium sulfate cement / silica-based mesoporous material composites for controlled release of BMP-2, Int. J. Nanomedicine. 10 (2015) 4341–4350. doi:10.2147/IJN.S85763.

[46] P.R.A.F. Garcia, R.N. Bicev, C.L.P. Oliveira, O.A.S. Anna, M.C.A. Fantini, Microporous and Mesoporous Materials Protein encapsulation in SBA-15 with expanded pores, Microporous Mesoporous Mater. 235 (2016) 59–68. doi:10.1016/j.micromeso.2016.07.033.

[47] A. Katiyar, S. Yadav, P.G. Smirniotis, N.G. Pinto, Synthesis of ordered large pore SBA-15 spherical particles for adsorption of biomolecules, J. Chromatogr. A. 1122 (2006) 13–20. doi:10.1016/j.chroma.2006.04.055.

[48] X. Diao, Y. Wang, Z. Junqi, S. Zhu, Effect of Pore-size of Mesoporous SBA-15 on Adsorption of Bovine Serum Albumin and Lysozyme Protein *, Chinese J. Chem. Eng. 18 (2010) 493–499. doi:10.1016/S1004-9541(10)60248-0.

[49] H.H.P. Yiu, C.H. Botting, N.P. Botting, P.A. Wright, Size selective protein adsorption on thiol-functionalised SBA-15 mesoporous molecular sieve, Phys. Chem. Chem. Phys. 3 (2001) 2983–2985. doi:10.1039/b104729a.

[50] G.J. de A.A. Soler-Illia, E.L. Crepaldi, D. Grosso, C. Sanchez, Block copolymer-templated mesoporous oxides, Curr. Opin. Colloid Interface Sci. 8 (2003) 109–126.

doi:10.1016/S1359-0294.

[51] O. Pagar, H. Nagare, Y. Chine, R. Autade, P. Narode, V. Sanklecha, Mesoporous Silica : A Review, Int. J. Pharm. Drug Anal. 6 (2019) 1–12.

[52] G.J.A.A. Soler-illia, P. Innocenzi, Mesoporous Hybrid Thin Films : The Physics and Chemistry Beneath, (2006) 4478–4494. doi:10.1002/chem.200500801.

[53] L. Zhao, H. Qin, R. Wu, H. Zou, Recent advances of mesoporous materials in sample preparation, J. Chromatogr. A. 1228 (2012) 193–204. doi:10.1016/j.chroma.2011.09.051.

[54] L. Cao, T. Man, M. Kruk, Synthesis of Ultra-Large-Pore SBA-15 Silica with Two-Dimensional Hexagonal Structure Using Triisopropylbenzene As Micelle Expander, Chem. Mater. 21 (2009) 1144–1153. doi:10.1021/cm8012733.

[55] L. Huang, M. Kruk, Journal of Colloid and Interface Science Synthesis of ultra-large-pore FDU-12 silica using ethylbenzene as micelle expander, J. Colloid Interface Sci. 365 (2012) 137–142. doi:10.1016/j.jcis.2011.09.044.

[56] H. Zhang, J. Sun, D. Ma, G. Weinberg, D.S. Su, X. Bao, Engineered Complex Emulsion System : Toward Modulating the Pore Length and Morphological Architecture of Mesoporous Silicas, (2006) 25908–25915.

[57] E.M. Johansson, J.M. Córdoba, M. Odén, Microporous and Mesoporous Materials The effects on pore size and particle morphology of heptane additions to the synthesis of mesoporous silica SBA-15, Microporous Mesoporous Mater. 133 (2010) 66–74. doi:10.1016/j.micromeso.2010.04.016.

[58] M. Kruk, Access to Ultralarge-Pore Ordered Mesoporous Materials through Selection of Surfactant / Swelling-Agent Micellar Templates, Acc. Chem. Res. 45 (2012) 1678–1687. doi:10.1021/ar200343s.

[59] G. V Deodhar, M.L. Adams, B.G. Trewyn, Controlled release and intracellular protein

delivery from mesoporous silica nanoparticles, Biotechnnology J. 12 (2017) 1600408. doi:10.1002/biot.201600408.

[60] R.J.P. Corriu, J.J.E. Moreau, P. Thepot, M. Wong Chi Man, New Mixed Organic-Inorganic Polymers: Hydrolysis and Polycondensation of Bis(trimethoxysilyl) organometallic Precursors, Chem. Mater. 4 (1992) 1217–1224. doi:10.1021/cm00024a020.

[61] N. Muramoto, T. Sugiyama, T. Matsuno, H. Wada, K. Kuroda, A. Shimojima, Preparation of Periodic Mesoporous Organosilica with Large Mesopores Using Silica Colloidal Crystals as Templates Received, Nanoscale. 12 (2020) 21155–21164. doi:10.1039/D0NR03837G.

[62] A. Birault, E. Molina, C. Carcel, J. Bartlett, N. Marcotte, G. Toquer, P. Lacroix-Desmazes, C. Gerardin, M. Wong Chi Man, Synthesis of lamellar mesostructured phenylene-bridged periodic mesoporous organosilicas (PMO) templated by polyion complex (PIC) micelles, J. Sol-Gel Sci. Technol. 89 (2019) 189–195. doi:10.1007/s10971-018-4667-1.

[63] M. Laird, C. Carcel, E. Oliviero, G. Toquer, P. Trens, J.R. Bartlett, M. Wong Chi Man, Single-template periodic mesoporous organosilica with organized bimodal mesoporosity, Microporous Mesoporous Mater. 297 (2020) 110042. doi:10.1016/j.micromeso.2020.110042.

[64] A. Lecloux, Texture of Catalysts, in: J.R. Anderson, M. Boudart (Eds.), Catal. Sci. Technol. Vol. 2, Springer, Berlin, 1981: p. 171. doi:10.1007/978-3-642-93247-2.

[65] S. Pirard, J. Mahy, J.-P. Pirard, B. Heinrichs, L. Raskinet, S. Lambert, Development by the sol–gel process of highly dispersed Ni–Cu/SiO2 xerogel catalysts for selective 1,2-dichloroethane hydrodechlorination into ethylene, Microporous Mesoporous Mater. 209 (2015) 197–207. doi:10.1016/j.micromeso.2014.08.015.

[66] A. Galarneau, F. Villemot, J. Rodriguez, F. Fajula, B. Coasne, Validity of the t - plot

Method to Assess Microporosity in Hierarchical Micro / Mesoporous Materials, Langmuir. 30 (2014) 13266–13274. doi:10.1021/la5026679.

[67] C.J. Gommes, B. Goderis, CONEX , a program for angular calibration and averaging of two-dimensional powder scattering patterns, J. Appl. Crystallogr. 43 (2010) 352–355. doi:10.1107/S0021889810001937.

[68] M. Zienkiewicz-Strzałka, M. Skibinska, S. Pikus, Small-angle X-ray scattering (SAXS) studies of the structure of mesoporous silicas, Nucl. Instruments Methods Phys. Res. B. 411 (2017) 72–77. doi:10.1016/j.nimb.2017.03.028.

[69] A. Galarneau, H. Cambon, F. Di Renzo, F. Fajula, True Microporosity and Surface Area of Mesoporous SBA-15 Silicas as a Function of Synthesis Temperature, Langmuir. 17 (2001) 8328–8335. doi:10.1021/la0105477.

[70] O.H. Lowry, N.J. Rosebrough, L.A. Farr, R.J. Randall, Protein measurement with the folin phenol reagent, J. Biol. Chem. 193 (1951) 265–275. doi:10.1016/0304-3894(92)87011-4.

[71] W.L. Huang, K.M. Liang, S.R. Gu, Calcining silica gels at different drying stages, (2000) 136–141.

[72] P.J. Davis, C.J. Brinker, D.M. Smith, Pore structure evolution in silica gel during aging / drying I . Temporal and thermal aging, J. Non. Cryst. Solids. 142 (1992) 189–196.

[73] P.J. Davis, C.J. Brinker, D.M. Smith, R.A. Assink, Pore structure evolution in silica gel during aging / drying II . Effect of pore fluids, J. Non. Cryst. Solids. 142 (1992) 197–207.

[74] S.-H. Wu, C.-Y. Mou, H.-P. Lin, Synthesis of mesoporous silica nanoparticles, Chem. Soc. Rev. 42 (2013) 3649–4258. doi:10.1039/c3cs35405a.

[75] H. Mansur, R. Oréfice, M. Pereira, Z. Lobato, FTIR and UV-vis study of chemically engineered biomaterial surfaces for protein immobilization, Spectroscopy. 16 (2002) 351–360. doi:10.1155/2002/183053.

[76] E. Péré, H. Cardy, O. Cairon, M. Simon, S. Lacombe, Quantitative assessment of organic compounds adsorbed on silica gel by FTIR and UV-VIS spectroscopies: the contribution of diffuse reflectance spectroscopy, Vib. Spectrosc. 25 (2001) 163–175. doi:10.1016/S0924-2031(00)00113-2.

[77] R. Antony, S. Theodore David Manickam, P. Kollu, P.V. Chandrasekar, K. Karruppasamy, S. Balakumar, Highly dispersed Cu(II), Co(II) and Ni(II) catalysts covalently immobilized on imine-modified silica for cyclohexane oxidation with hydrogen peroxide, RSC Adv. 4 (2014) 24820–24830. doi:10.1039/C4RA01960A.

[78] L.B. Capeletti, I.M. Baibich, I.S. Butler, J.H.Z. dos Santos, Infrared and Raman spectroscopic characterization of some organic substituted hybrid silicas, Spectrochim. Acta Part A Mol. Biomol. Spectrosc. 133 (2014) 619–625. doi:10.1016/j.saa.2014.05.072.

[79] J. Osswald, K.T. Fehr, FTIR spectroscopic study on liquid silica solutions and nanoscale particle size determination, J. Mater. Sci. 41 (2006) 1335–1339. doi:10.1007/s10853-006-7327-8.

[80] S.L. Warring, D.A. Beattie, A.J. Mcquillan, Sur fi cial Siloxane-to-Silanol Interconversion during Room- Temperature Hydration/Dehydration of Amorphous Silica Films Observed by ATR-IR and TIR-Raman Spectroscopy, Langmuir. 32 (2016) 1568–1576. doi:10.1021/acs.langmuir.5b04506.

[81] M. Etienne, A. Walcarius, Analytical investigation of the chemical reactivity and stability of aminopropyl-grafted silica in aqueous medium, Talanta. 59 (2003) 1173–1188. doi:10.1016/S0039-9140(03)00024-9.

[82] A. Célino, O. Gonc, F. Jacquemin, S. Fréour, Qualitative and quantitative assessment of water sorption in natural fibres using ATR-FTIR spectroscopy, Carbohydr. Polym. 101 (2014) 163–170. doi:10.1016/j.carbpol.2013.09.023.

[83] L. Adumeau, C. Genevois, L. Roudier, C. Schatz, L. Adumeau, C. Genevois, L. Roudier, C. Schatz, F. Couillaud, Impact of surface grafting density of PEG macromolecules on dually fluorescent silica nanoparticles used for the in vivo imaging of subcutaneous tumors, Biochim. Biophys. Acta. 1861 (2017) 1587–1596. doi:10.1016/j.bbagen.2017.01.036.

[84] S. Bharathi, N. Fishelson, O. Lev, Direct Synthesis and Characterization of Gold and Other Noble Metal Nanodispersions in Sol - Gel-Derived Organically Modified Silicates, Langmuir. 15 (1999) 1929–1937. doi:10.1021/la980490x.

[85] L.T. Zhuravlev, Concentration of Hydroxyl Groups on the Surface of Amorphous Silicas, Langmuir. 3 (1987) 316–318. doi:10.1021/la00075a004.

[86] S. Mohan, N. Sundaraganesan, J. Mink, FTIR and Raman studies on benzimidazole, Spectrochim. Acta. 47A (1991) 1111–1115. doi:10.1016/0584-8539(91)80042-H.

[87] Y.S. Mary, P.. J. Jojo, C.Y. Panicker, C. Van Alsenoy, S. Ataei, I. Yildiz, Quantum mechanical and spectroscopic (FT-IR , FT-Raman , 1H NMR and UV) investigations of 2-(phenoxymethyl) benzimidazole, Spectrochim. Acta Part A Mol. Biomol. Spectrosc. 125 (2014) 12–24. doi:10.1016/j.saa.2014.01.068.

[88] J. Coates, Interpretation of Infrared Spectra , A Practical Approach, in: R.A. Meyers (Ed.), Encycl. Anal. Chem., John Wiley & Sons Ltd, Chichester, 2000: pp. 10815–10837. doi:10.1002/9780470027318.

[89] P. Trens, R. Denoyel, E. Guilloteau, Evolution of Surface Composition , Porosity , and Surface Area of Glass Fibers in a Moist Atmosphere, Langmuir. 12 (1996) 1245–1250. doi:10.1021/la950531e.

[90] M.T.J. Keene, R.D.M. Gougeon, R. Denoyel, R.K. Harris, J. Rouquerola, P.L. Llewellyn, Calcination of the MCM-41 mesophase: mechanism of surfactant thermal degradation and

evolution of the porosity, J. Mater. Chem. 9 (1999) 2843–2850. doi:10.1039/A904937A.

[91] N. Rose, M. Le Bras, R. Delobel, B. Costes, Y. Henry, Thermal oxidative degradation of an epoxy resin, Polym. Degrad. Stab. 42 (1993) 307–316. doi:10.1016/0141-3910(93)90226-9.

[92] G. Temtsin, T. Asefa, S. Bittner, G.A. Ozin, Aromatic PMOs: tolyl, xylyl and dimethoxyphenyl groups integrated within the channel walls of hexagonal mesoporous silicas, J. Mater. Chem. 11 (2001) 3202–3206. doi:10.1039/B103960C.

[93] E. Russo, C. Villa, Poloxamer Hydrogels for Biomedical Applications, Pharmaceutics. 11 (2019) 671. doi:10.3390/pharmaceutics11120671.

[94] P. Singla, O. Singh, S. Sharma, K. Betlem, V.K. Aswal, M. Peeters, R.K. Mahajan, D. Building, C. Street, M. Manchester, Temperature-Dependent Solubilization of the Hydrophobic Antiepileptic Drug Lamotrigine in Di ff erent Pluronic Micelles □ A Spectroscopic , Heat Transfer Method , Small-Angle Neutron Scattering , Dynamic Light Scattering , and in Vitro Release Study, ACS Omega. 4 (2019) 11251–11262. doi:10.1021/acsomega.9b00939.

[95] J. Bhattacharjee, B. Atomic, G. Verma, B. Atomic, V.K. Aswal, B. Atomic, V.B. Patravale, Microstructure, drug binding and cytotoxicity of Pluronic P123–aerosol OT mixed micelles, RSC Adv. 3 (2013) 23080–23089. doi:10.1039/c3ra44983a.

[96] Y. Duan, X. Cai, H. Du, G. Zhai, Novel in situ gel systems based on P123 / TPGS mixed micelles and gellan gum for ophthalmic delivery of curcumin, Colloids Surfaces B Biointerfaces. 128 (2015) 322–330. doi:10.1016/j.colsurfb.2015.02.007.

[97] L.-Y. Zhao, W.-M. Zhang, Recent progress in drug delivery of pluronic P123 : pharmaceutical perspectives, J. Drug Target. 25 (2017) 471–484. doi:10.1080/1061186X.2017.1289538.

[98] M. Thommes, K. Kaneko, A. V Neimark, J.P. Olivier, F. Rodriguez-Reinoso, J. Rouquerol, K.S.W. Sing, Physisorption of gases, with special reference to the evaluation of surface area and pore size distribution (IUPAC Technical Report), Pure Appl. Chem. 87 (2015) 1051–1069. doi:10.1515/pac-2014-1117.

[99] S. Manet, J. Schmitt, M. Impéror-Clerc, V. Zholobenko, D. Durand, C.L.P. Oliveira, J.S. Pedersen, C. Gervais, N. Baccile, F. Babonneau, I. Grillo, F. Meneau, C. Rochas, Kinetics of the Formation of 2D-Hexagonal Silica Nanostructured Materials by Nonionic Block Copolymer Templating in Solution, J. Phys. Chem. B. 115 (2011) 11330–11344. doi:10.1021/jp200213k.

[100] A. Sundblom, C.L.P. Oliveira, J.S. Pedersen, A.E.C. Palmqvist, On the Formation Mechanism of Pluronic-Templated Mesostructured Silica, J. Phys. Chem. C. 114 (2010) 3483–3492. doi:10.1021/jp100087z.

[101] Y. Zhou, G. Quan, Q. Wu, X. Zhang, B. Niu, Mesoporous silica nanoparticles for drug and gene delivery, Acta Pharm. Sin. B. 8 (2018) 165–177. doi:10.1016/j.apsb.2018.01.007.

[102] E. Serra, E. Díez, I. Díaz, R.M. Blanco, A comparative study of periodic mesoporous organosilica and different hydrophobic mesoporous silicas for lipase immobilization, Microporous Mesoporous Mater. 132 (2010) 487–493. doi:10.1016/j.micromeso.2010.03.031.

[103] M. Vallet-Regí, M. Colilla, I. Izquierdo-Barba, M. Manzano, Mesoporous Silica Nanoparticles for Drug Delivery : Current Insights, Molecules. 23 (2018) 47. doi:10.3390/molecules23010047.

Data availability

The raw/processed data required to reproduce these findings cannot be shared at this time as the data also forms part of an ongoing study.

Graphical abstract

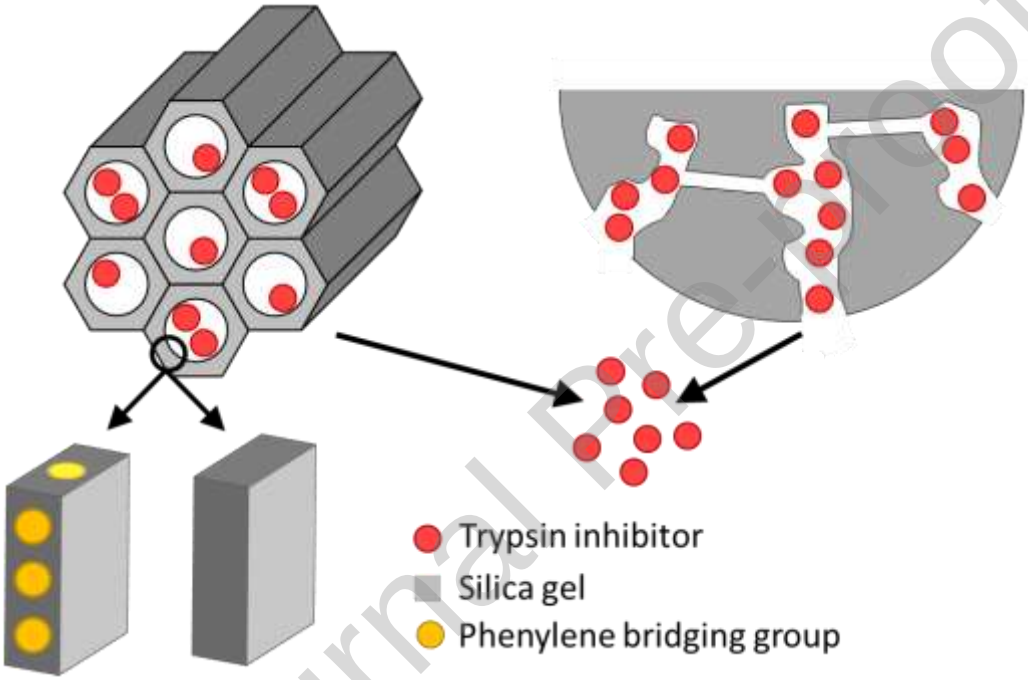

Author Contributions:

Conceptualization, methodology, writing, R.G.T., J.G.M., A.P.F.M., A.B.; investigation and analysis, R.G.T., J.G.M., A.P.F.M., A.B., J.F., M.L., C.C., N.R., and B.G., writing-original draft preparation, R.G.T.; supervision, funding acquisition and project administration, C.G., M.W.C.M., and S.D.L. All the authors corrected the paper before submission and during the revision process.

Declaration of interests

☒ The authors declare that they have no known competing financial interests or personal relationships that could have appeared to influence the work reported in this paper.

☐The authors declare the following financial interests/personal relationships which may be considered as potential competing interests:

Highlights

- SBA-15 and SMS silica materials synthesized with hydrothermal method
- Swelling agent added with TEOS led to ordered mesoporous silica
- Unstructured sample showed a higher protein loading and a higher protein release
- Structured sample produced a steady release over time
- Hydrophobicity of the silica surface plays a major role on the protein encapsulation and its release rate.